# Statistical and Temporal Characterization of Turbulent Rayleigh-Bénard Convection Boundary Layers Using Time-Resolved PIV Measurements

**Christian E. Willert, Ronald du Puits and Christian Resagk**

**Abstract**  This contribution reports on near-wall flow field measurements in turbulent Rayleigh-Bénard convection (RBC) in air at a fixed Prandtl number $Pr = 0.7$ and Rayleigh number $Ra = 1.45 \times 10^{10}$. For the experiment, the large-scale convection (LSC) was confined to a rectangular box of $2.5 \times 2.5 \times 0.65\,\mathrm{m}^3$ made of transparent acrylic sheets. Prior video-graphic visualizations of the bottom boundary layer flow by means of laser light sheet illumination of small particles indicated the presence of highly dynamic flow behaviour at flow conditions that classical stability analysis predicts to still be in the laminar regime. While theory predicts a transition to turbulence at Reynolds numbers $Re_\delta \approx 420$, the present investigation exhibits highly unsteady flow at a much lower Reynolds number of $Re_\delta \approx 260$ based on boundary layer thickness. With the help of the PIV data, it can be demonstrated that the entrainment of turbulent structures from the mean wind into the boundary layer acts, alongside with the destabilization due to inner shear, as a second mechanism on its path to turbulence. Both contributions must be considered when predicting the critical bound towards the *ultimate regime* of thermal convection. The measurements rely on the acquisition of long, continuous sequences of particle image velocimetry (PIV) data from which both statistical and spectral information can be retrieved. Contrary to conventional implementation of the PIV technique the field of view is restricted to a narrow strip, generally extending in wall-normal direction. In this way, both the acquisition frequency and the total number images of the employed high-speed camera are proportionally increased. The temporally oversampled data allows the use of multi-frame PIV processing algorithms which reduce measurement uncertainties with respect to standard dual-frame analysis.

C.E. Willert (✉)
DLR Institute of Propulsion Technology, German Aerospace Center,
51170 Köln, Germany
e-mail: chris.willert@dlr.de

R. du Puits · C. Resagk
Department of Mechanical Engineering, Technische Universität Ilmenau,
P.O. Box 100565, 98684 Ilmenau, Germany
e-mail: ronald.dupuits@tu-ilmenau.de

C. Resagk
e-mail: christian.resagk@tu-ilmenau.de

317

# 1 Introduction

Many natural or technical flows are associated with a heat transfer from hot or cold surfaces to the surrounding fluid. Because of its rather controllable boundary conditions—a confined fluid cooled from above and heated from below—Rayleigh-Bénard convection (RBC) has been the subject of numerous studies in the past decades, both numerically and experimentally (for a comprehensive review, see Ahlers et al. [1]). However, particularly in the case of turbulent RBC, the knowledge about the temperature and velocity field inside the convective boundary layer is still rather limited, which in turn affects the predictability of the local heat transfer coefficient. This process can be investigated experimentally in the "Barrel of Ilmenau" [5], a large facility which offers both high Rayleigh numbers and large flow scales with boundary layer thicknesses in the tens of millimetre range. Especially, the latter property permits a maximum of spatial resolution for established optical and probe-based measurement techniques.

Previous measurements in the facility recovered both the temperature and velocity profiles on the top and bottom walls using glass-encapsulated microthermistors [2] and laser Doppler anemometry (LDA) [3, 10]. While these single-point measurements provide valuable flow statistics, they only give limited insight to the topology of the flow. In this regard, planar techniques such as particle image velocimetry (PIV) are methods of choice yet so far have found little application in high-Ra Rayleigh-Bénard convection in air ($Pr = 0.7$), and to our knowledge have not been applied for the detailed investigation of the transitional boundary layers.

Extensive PIV measurements of both the global flow field as well as the boundary layer structure have been performed Zhou and Xia [16] and Sun et al. [12] in smaller scale facilities for similar Ra numbers with water as working fluid ($Pr = 4.3$). In these works, continuous PIV sequences in excess of 4 h were recorded at sample rates of 2.2 Hz. Among the findings was that the intermittent emissions of coherent structures caused by thermal plumes do not modify the Blasius-type laminar velocity profile which indicates that heat transfer across the thermal boundary layer is mainly by conduction. Modification of this heat transfer is expected with the onset of turbulence. Based on the Prandtl-Blasius theory of a flat-plate boundary layer and the stability criterion $Re = U \delta/\nu = 420$ derived by Tollmien [13], the transition in heat transfer in turbulent RBC was firstly predicted by Kraichnan [9] and later on defined more precisely by Grossmann and Lohse [8]. The latter authors predict a critical Ra number of $Ra_c \approx 10^{13} \ldots 10^{14}$ as the stability criterion in turbulent RBC at $Pr = 0.7$.

Video-graphic visualizations of the bottom boundary layer in the "Barrel of Ilmenau" facility by means of laser light sheet illumination of small particles indicated the presence of highly dynamic flow behaviour at flow conditions that classical stability analysis predict to still be in the laminar regime [4, 6]. The Reynolds number of the present investigation is $Re_\delta \approx 260$ which is considerably lower than the predicted transition Reynolds number of $Re_\delta \approx 420$. Also the corresponding Rayleigh number of $Ra = 1.45 \times 10^{10}$ is well below the extrapolated value of $Ra \approx 2 \times 10^{13}$ reported by Sun et al. [12]. In their measurements, they observed a clear departure of the

time-averaged data from the Prandtl-Blasius laminar boundary layer profile which would be indicative of a transitional behaviour. However, Zhou and Xia [16] pointed out that a normalization of the velocity profile by the instantaneous viscous boundary layer thickness $\delta_\nu$ results in a good agreement with the predicted Prandtl-Blasius profile.

In an effort to elucidate the transient behaviour of the boundary layer and to augment existing time-averaged data [10], the following article presents results obtained with long, time-resolved sequences of the bottom boundary layer in the "Barrel of Ilmenau" large-scale RBC facility. The first part of this contribution describes the experimental methods using time-resolved PIV for investigation of turbulent flows. These methods form the basis for the characterization of the boundary layer of turbulent Rayleigh-Bénard convection provided in the second and main part of the article.

## 2 Time-Resolved PIV for Near-Wall Flow Measurement

The investigation of turbulent flows in general strongly depends on gain information on the statistics of the flow. For the experimental investigation of wall bounded flow, this requirement is fulfilled by hot wire anemometry (HWA) and laser Doppler anemometry (LDA) as these are capable of providing measurement data with both high temporal and spatial resolution. On the other hand, particle image velocimetry (PIV) captures snapshots of the flow field—even volumetric—and thereby provides valuable information on the topology of the flow. PIV has been used extensively for the investigation of turbulent flows essentially ever since the time it has been developed. Due to the spatial averaging nature and rather low sampling rate (typ < 1 kHz), PIV generally has significant limitations in providing statistical information comparable to HWA and LDA. Nonetheless, current technology allows the technique to be pushed to higher sampling rates by reducing the spatial resolution of the sensor and focussing on a particular area of interest with increased magnification. Rather than capturing 2-D or 3-D maps of the flow field, the implementation of PIV utilized for the present investigation is aimed at obtaining measurement data along a narrow strip with a high number of samples at acquisition rates matching the time scales of the flow. In effect, this approach has the potential of bridging the gap between single-point measurement techniques (e.g. HWA, LDA) and conventional PIV, and shall be the main subject of this contribution.

## 2.1 Near-Wall Measurement of Turbulent Wall Flow

Reliable near-wall measurements with high frame rate PIV become feasible when the magnification of imaging system exceeds resolutions in the range of one pixel per wall unit ($z^+$) and the frame-to-frame displacements are limited to a few tens of

pixels. While this becomes increasingly challenging with higher Reynolds number, the measurements presented here have viscous sublayer thicknesses in the millimetre range such that conventional imaging optics (macro lenses) can be used. At the same time, the outer velocities typically are below 1 m/s which requires camera frame rates of 100–200 Hz to keep frame-to-frame displacements within bounds.

From a hardware point of view, the measurement setup is rather straightforward as it can be reduced to a medium-speed camera and a continuous wave laser of 2–5 W radiant power. The laser light is formed into a narrow, thin light sheet and is directed into the facility at a wall-normal direction, ideally through a clean glass surface. This narrow strip is then imaged by the high-speed camera, whose electronic shutter prevents excessive particle streaking on the sensor.

The technique was first applied for the investigation of the developing turbulent boundary layer of the air flow inside a square rectangular duct with $\mathrm{Re}_D = 20,000$ and $\mathrm{Re}_\delta = 4,900$ using image sequences with lengths up to $N \approx 180,000$ at frame rates of 10–50 kHz [15]. While the high sample count ensures statistical convergence, the time-resolved nature of the data allows the estimation of both velocity spectra and space-time correlations.
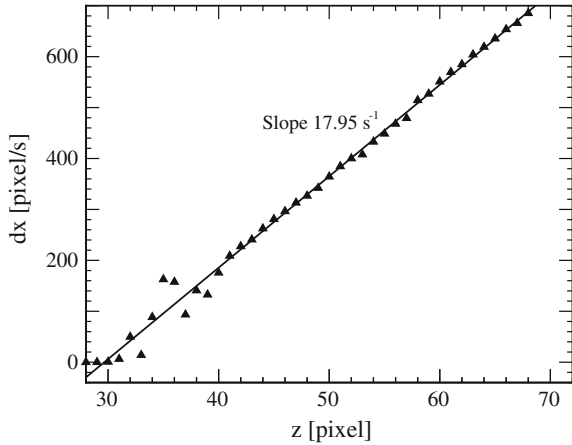
## *2.2 Estimation of the Wall Shear Rate*

Wall shear stress is directly linked to the wall shear rate, that is, the velocity gradient $\dot{\gamma} = du/dz$ at the wall:

$$\tau_{\mathrm{w}} = \mu \frac{du}{dz}\bigg|_{y=0}. \tag{1}$$

To recover estimates of the wall, shear stress using particle-based imaging methods requires that the linear portion of the sublayer is sufficiently well resolved such that the gradient can be obtained through finite differing of velocity estimates. Within the linear region, the fluid motion and along with it the motion of the particles is wall parallel. Therefore, it is possible to limit the frame-to-frame displacement estimation to recover only the wall-parallel motion. With the camera properly aligned, this can be achieved by cross-correlating single rows of wall-parallel pixels.

Figure 1 shows the mean wall-parallel velocity of particles within 30 pixels from the wall. Aside from deviations really close to the wall, caused by stationary particles or dust on the wall, the profile is linear throughout owing to the nearly 5-mm-thick viscous sublayer of the RBC boundary layer. The slope of a linear fit to this linear portion provides an estimate of the wall shear rate $\dot{\gamma}_w = du/dz$ and can be used for the straightforward calculation of the friction velocity $u_\tau$ and associated normalization factors. For a value of $\dot{\gamma}_w \approx 17.95\,\mathrm{s}^{-1}$ deduced from Fig. 1, this yields

**Fig. 1** Mean near-wall particle velocity obtained by single-line image cross-correlation. The wall is approximately located at 29 pixel and magnification is 45.7 μm/pixel

$$u_\tau = \sqrt{\frac{\tau_\mathrm{w}}{\rho}} = \sqrt{\nu \frac{du}{dz}\Big|_{y=0}} \approx 17.1 \,\mathrm{mm/s} \tag{2}$$

$$\frac{x_i^+}{x_i} = \frac{u_\tau}{\nu} \approx 1.05 \mathrm{mm}^{-1}. \tag{3}$$

While Fig. 1 provides mean values, the single-line cross-correlation technique can also be used to estimate the instantaneous wall shear rate and with it the time varying wall shear stress $\tau_w$ [15].

## 3 Near-Wall Measurements of Rayleigh-Bénard Convection

Turbulent Rayleigh-Bénard convection (RBC) is initiated in a confined fluid in the presence of a sufficiently strong temperature difference between a cooler top surface and a warmer bottom surface. The present measurements are aimed at gaining further insight on the transient behaviour of the boundary layer on the bottom wall previously observed through visualization by du Puits et al. [6]. The acquisition of long PIV image sequences of up to $N \approx 59{,}000$ samples are motivated by achieving both statistical convergence as well as providing continuous time records of the transient flow.

### 3.1 Experimental Facility and Operating Conditions

For the experiment, the large-scale convection is confined to a rectangular box of $2.5 \times 2.5 \times 0.65\,\mathrm{m}^3$ made of transparent acrylic sheets Fig. 2. The temperature difference between the bottom and top wall is $\Delta T = 10\,\mathrm{K}$. With air as the working
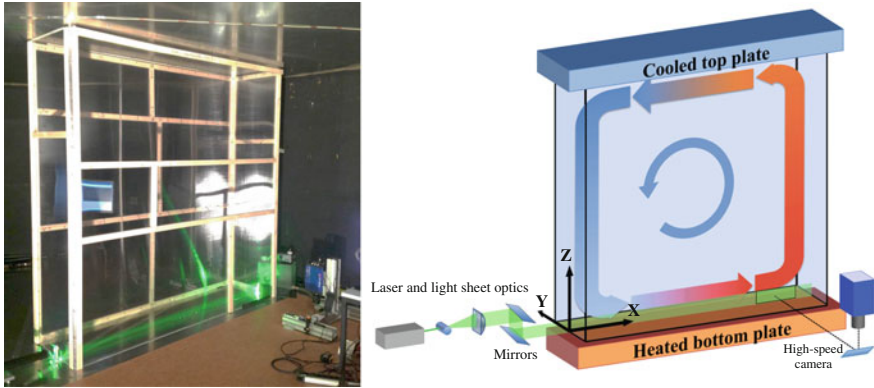
**Fig. 2** PIV imaging setup for the investigation of RBC within a confined rectangular cell inside the *Barrel of Ilmenau*. *Right* schematic of the global flow pattern within the RBC cell, PIV measurement setup and coordinate system

fluid (Pr = 0.7) the Rayleigh number amounts to Ra $= 1.45 \times 10^{10}$. Further details of the facility itself are given in [5].

## 3.2 Data Acquisition in the RBC Facility

To obtain more detailed information on the statistics and the temporal evolution of the boundary layer flow, long PIV image sequences were recorded at various positions near the centerline of the heated bottom plate (Fig. 2). Laser light sheet illumination was realized with a 2 W continuous wave laser. The light sheet thickness was approximately 1–2 mm with a uniform height of approximately 70 mm across the horizontal length of 2.5-m-wide cell. A smoke generator, based on an evaporation–condensation principle, was used to seed the flow with 1–2 $\mu$m oil droplets whose life time exceeded 1 h.

Images of the illuminated particles were acquired with a high-speed camera (*PCO GmbH, Dimax-S4*) at a frame rate of 200 Hz and a spatial resolution of 2016 × 600 pixels. With the camera positioned upright, a 90° mirror in front of the macrolens (*Zeiss Macro-Planar 100/2*) aligned the optical axis with the normal to the light sheet. Aside from its high light sensitivity, the main benefits of this camera are its large dynamic range of 12 bits and large internal storage to capture long sequences of more than 20,000 frames at the chosen resolution. Particle streaking by the CW illumination could be reduced by limiting the sensor exposure to 2 ms.

As indicated in Table 1, various image sequences at two magnifications were captured, one to obtain the global features of the boundary layer and a second, higher resolution to retrieve selected profiles with improved statistical convergence. A high magnification of up to 22.1 pixel/mm was chosen in order to resolve the viscous sublayer (a wall unit corresponds to roughly $z^+/z = 1$ mm, see Table 2). To increase

**Table 1** Imaging parameters for the acquired PIV sequences of near-wall RBC

|  | Symbol | Overview | Detailed view A, B, C, D | Unit |
|---|---|---|---|---|
| Magnification | $m$ | 9.1 | 22.1 | pixel/mm |
| Field of view | $[W \times H]$ | $220 \times 65$ | $13 \times 68$ | mm$^2$ |
|  | $[W \times H]$ | $2016 \times 600$ | $288 \times 1500$ | pixel |
| Camera frame rate | $f_{\mathrm{acq}}$ | 200 | 100/200 | Hz |
| Camera exposure | $t_{\mathrm{exp}}$ | 2.0 | 2.0 | ms |
| Duration | $t_{\mathrm{seq}}$ | 106 | 592/296 | s |
| Number of frames | $N$ | 21161 | 59235 |  |

**Table 2** Boundary layer data obtained for measurement positions A through D

|  |  | A | B | C | D | Unit |
|---|---|---|---|---|---|---|
| Position | $x/L$ | 0.09 | 0.48 | 0.64 | 0.92 | – |
| Boundary layer thickness | $\delta$ | 22.8 | 32.8 | 35.8 | 62.9 | (mm) |
| Boundary layer thickness | $\delta_{99\%}$ | 18.7 | 25.3 | 27.7 | 51.3 | (mm) |
| Kinematic boundary layer thickness | $\delta_\nu$ | 8.05 | 9.82 | 10.9 | 21.6 | (mm) |
| Displacement thickness | $\delta_*$ | 5.32 | 6.78 | 7.54 | 14.3 | (mm) |
| Momentum thickness | $\theta$ | 2.49 | 3.06 | 3.45 | 6.13 | (mm) |
| Shape factor | $S = \delta_*/\theta$ | 2.14 | 2.22 | 2.18 | 2.34 | – |
| Maximum velocity | $U_{\mathrm{max}}$ | $-37.8$ | 169 | 155 | 83.2 | (mm s$^{-1}$) |
| Wall shear rate | $\dot{\gamma}_w = \frac{du}{dy}$ | 3.83 | 16.7 | 13.7 | 2.85 | (s$^{-1}$) |
| Friction velocity | $u_\tau$ | 7.88 | 16.4 | 14.9 | 6.79 | (mm s$^{-1}$) |
| Wall unit | $z^+/z$ | 0.486 | 1.015 | 0.920 | 0.419 | (mm$^{-1}$) |
| Reynolds number | $\mathrm{Re}_\delta$ | (53.2) | 343 | 343 | 323 | – |
| Reynolds number | $\mathrm{Re}_{\delta_{99}}$ | (43.8) | 264 | 265 | 263 | – |
| Reynolds number | $\mathrm{Re}_{\delta_\nu}$ | (18.8) | 103 | 104 | 111 | – |

the duration of the acquisition, one sequence was acquired at 100 Hz which also doubled the particle displacements to a level comparable to the light sheet thickness. As a consequence, the loss of signal due to out-of-plane particle motion increased and required careful adjustment of PIV processing parameters.

## 3.3 PIV Analysis and Data Post Processing

The acquired image sequences were processed pair-wise with conventional PIV processing software (PIVTEC GmbH, PIVview2C, v3.5) using sample sizes of $24 \times 16$ pixels ($W \times H$) and $64 \times 8$ pixels at 50% overlap, where the latter sample size was chosen to improve the resolution in the presence of strong, near-wall shearing motions. The recovered velocity data was additionally temporally filtered using a Gaussian weighted averaging kernel to reduce noise in the individual velocity estimates. The chosen kernel width of 6 frames ($e^{-2}$) corresponds to a temporal filter width of 30 ms, which is well below the smallest time scales present in this flow. For example, at Ra $= 1.45 \times 10^{10}$, the Kolmogorov length scale is $\eta \approx 4.4$ mm with a time scale $\tau \approx 1.2$ s.

Figure 3 provides an overview of the acquired measurement domains. The four narrow (red) stripes indicate positions that were imaged with higher resolution and an increased number of samples (nearly 60,000 images each). Each of the twelve sampling areas were acquired with a pause of about 30 min in between, which to a large extent is due to the time required to download images from the camera as well as camera repositioning and length calibration. Figure 4 provides the mean velocity distribution at three relevant positions, namely the impingement area of the downwelling flow near the right corner (A), a position near the middle where the boundary layer is considered to be well established (C), and finally an area near the right corner where the mean flow is directed upward (D).
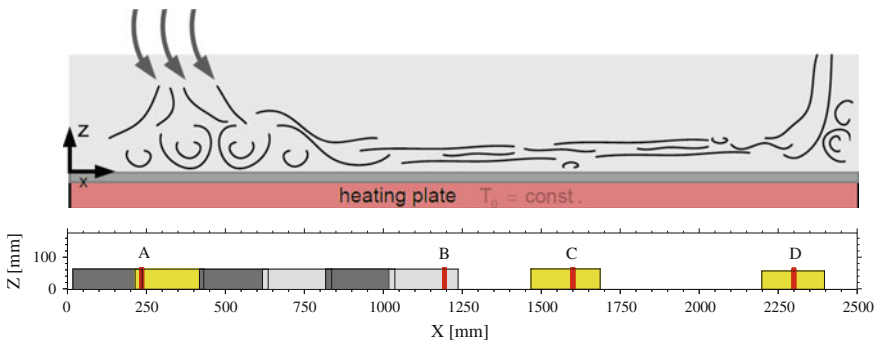


**Fig. 3** Schematic of flow field (*top*) and overview of PIV measurement areas. The *narrow vertical strips* labelled A,B,C and D indicate areas used for profile measurements. Flow fields for the *yellow* areas are provided in Fig. 4
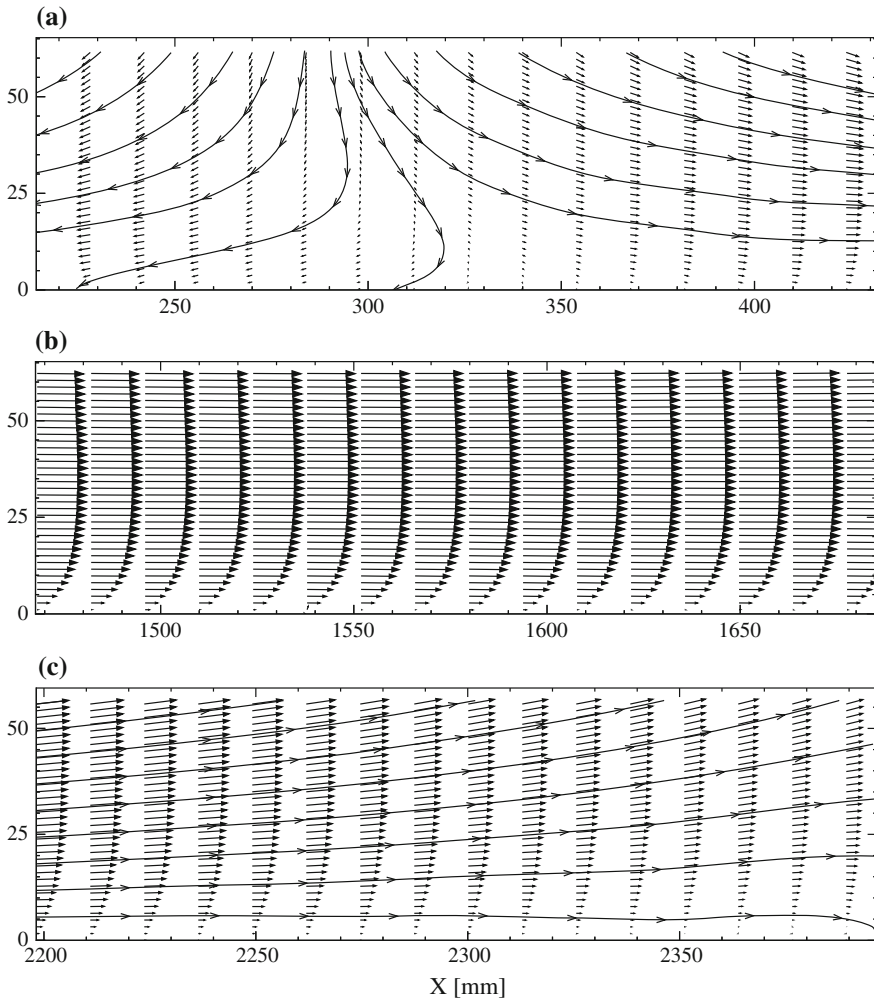
**(a)**

**(b)**

**(c)**

X [mm]

**Fig. 4** Overview of mean velocity field at three positions along centerline: downwelling region (**a**), middle area (**b**), and upwelling region (**c**); vectors desampled 16× horizontally, 2× vertically

The flow near the left corner (Fig. 4) is clearly dominated by downward motion and even reverses with a clearly visible stagnation point at $x \approx 330$ mm. The flow then accelerates with increasing horizontal distance establishing a boundary layer with a maximum velocity of $U_{\max} \approx 160–170$ mm/s at a wall distances of $z = 30–35$ mm. Towards the right corner, the mean streamlines indicate the deflection of the horizontal shear flow towards the upper plate by the vertical sidewall.

In order to estimate the mean wall shear rate $\dot{\gamma}_w$, a modified PIV processing scheme is used that employs cross-correlation on single line of pixels (wall parallel). The procedure is described in Sect. 2.2 and provides velocity estimates at
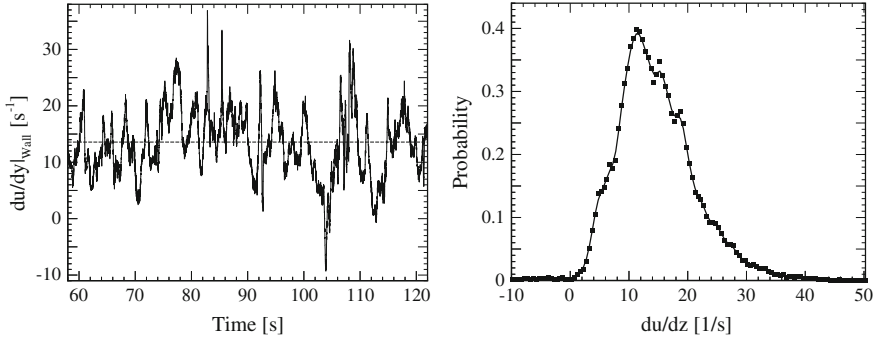
**Fig. 5** Temporal evolution (12,000 samples) and probability density function (*right*) of the wall shear rate $\dot{\gamma}_w = du/dz$ at $x/L = 0.64$ (mean: $13.7\,\mathrm{s}^{-1}$, $\sigma : 6.8\,\mathrm{s}^{-1}$, skew: 0.51)

single-pixel increments with a wall-normal resolution of one pixel ($45.2\,\mu\mathrm{m}$). A linear least squares fit over these estimates provides the near-wall velocity gradient in units of [pixel/pixel], and hence is dimensionless. Division by the time differ-ence between image recordings provides the wall shear rate. This gradient can be obtained for each image pair such that the statistics and temporal evolution can be further analysed. A two-minute portion of the highly fluctuating wall shear rate is shown in Fig. 5, left. The probability density function for the entire record is given in Fig. 5, right. A positive skew is indicative of the intermittent behaviour as shown by the high-amplitude bursts in the time trace.

## 4 Results and discussion

The characteristic values for the four detailed boundary layer measurement areas are summarized in Table 2. Profiles of the normalized mean velocity profile at two posi-tions are provided in Fig. 6. At position $x/L = 0.48$, the maximum velocity $U_{\max} = 169\,\mathrm{mm/s}$ is reached at a wall distance of $\delta = 32.8\,\mathrm{mm}$. At greater wall distances, the mean velocity slowly decays. Further downstream ($x/L = 0.64$, $x/L = 0.92$) the boundary layer thickens, while the maximum velocity reduces; the Reynolds number stays approximately constant. This indicates that the boundary layer does not receive additional momentum from the outer flow aside from the momentum added in the downwelling region at $x/L \lesssim 0.3$. At $x/L = 0.92$, the mean velocity profile exhibits a reduced velocity gradient at the wall which is caused by the separating flow in this area (Fig. 8).

The velocity profiles also clearly deviate from the laminar Prandtl-Blasius profile which corresponds to results reported for DNS [11, 14] as well as previous LDA measurements [2, 10, 16]. In Fig. 6, the viscous sublayer is present where the profile follows the Prandtl-Blasius profile and begins to depart at $z/\delta \gtrsim 0.1$ corresponding
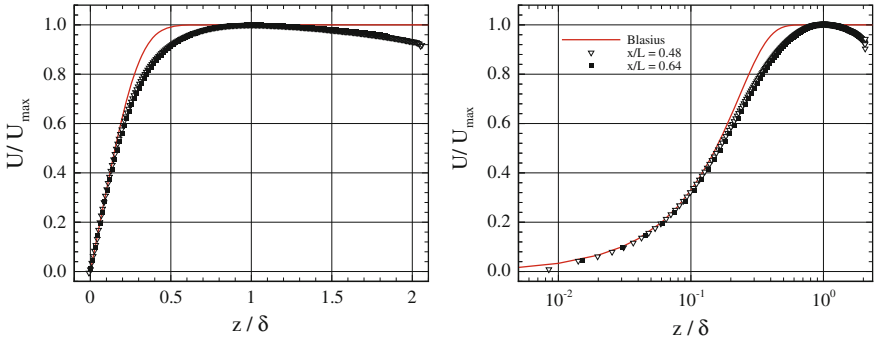
**Fig. 6** Wall-normal distribution of the mean horizontal velocity at $x/L = 0.48$ ($\triangledown$) and $x/L = 0.64$ with mean velocities of $U_{max} = 169\,\text{mm/s}$ and $U_{max} = 155\,\text{mm/s}$ at wall distances $\delta = 32.3\,\text{mm}$ and $\delta = 35.8\,\text{mm}$, respectively
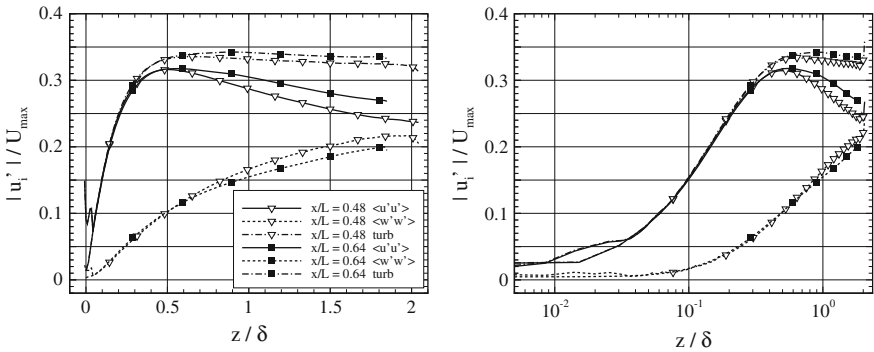


**Fig. 7** Wall-normal distribution of fluctuating components at $x/L = 0.48$ ($\triangledown$) and $x/L = 0.64$

to $z^+ \approx 4$. However, a fully developed logarithmic region does not exist in the mean velocity profile (Fig. 6, right) due to the transitional character of the boundary layer.

The wall-normal distribution of the time-averaged fluctuating velocity components $\langle u_i' u_j' \rangle$ is shown in Fig. 7. While the horizontal fluctuations $u'$ reach a maximum at a normalized wall distance $z/\delta \approx 0.5$ corresponding roughly to $16\,z^+$ and decay after that, the vertical fluctuations $w'$ continue to increase asymptotically approaching the value of the horizontal fluctuations. This indicates increasing isotropy of the fluid motion (or turbulence) with increased wall distance. The combined quantity—the square root of their sum—reaches at constant value near $z/\delta \approx 0.5$ and only slightly decays thereafter which suggests near constant turbulent kinetic energy in the outer regions of the boundary layer.

The planar nature of PIV data allows the retrieval of differential quantities that are difficult to obtain with single-point techniques such as laser Doppler anemometry (LDA) and hotwire anemometry (HWA). As an example, Fig. 9 shows the wall-normal distribution of mean and fluctuating values of the out-of-plane vorticity
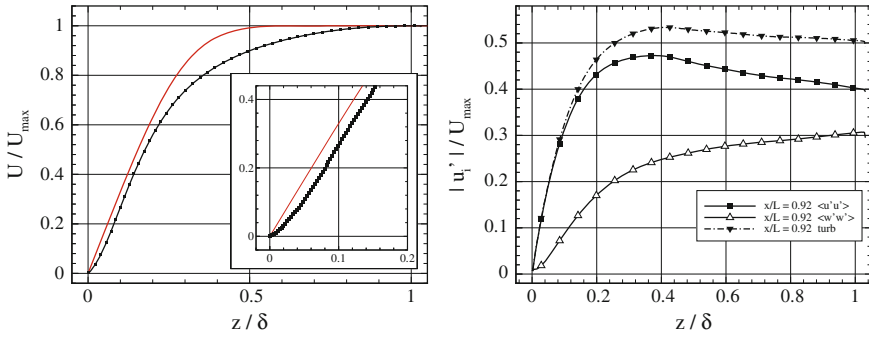
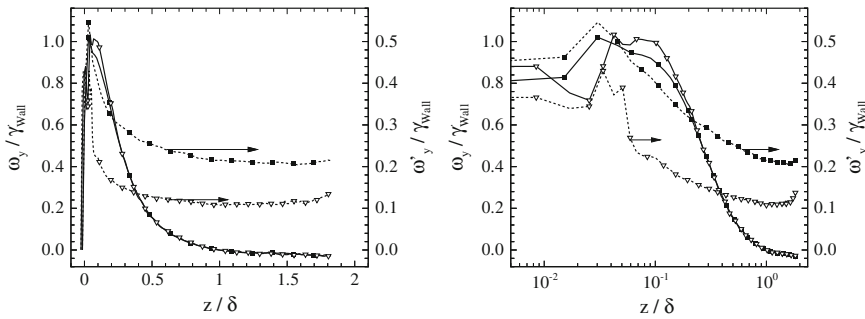**Fig. 8** Wall-normal distribution of mean horizontal velocity (*left*) and fluctuations (*right*) at $x/L = 0.92$

**Fig. 9** Wall-normal distribution of mean and fluctuations of vorticity component $\omega_y$ at $x/L = 0.48$ ($\triangledown$) and $x/L = 0.64$

component $\omega_y$. Normalized by the wall shear rate, its value peaks near the wall at about $\omega/\dot{\gamma}_w = 0.4$. Closer to the wall, the measurement uncertainty increases due to light scattering at the surface, which "locks" the displacement to zero. Correspondingly, the RMS value of vorticity decays in the immediate vicinity of the wall for $z/\delta < 0.1$, which is not representative. Compared to the velocity fluctuations (Fig. 6, right), the strongest vorticity fluctuations occur much closer to the wall and have nearly decayed to levels close of the outer flow.

While the previous results focussed on the statistics of the boundary layer flow, we will now highlight some of temporal characteristics of the flow. Figure 11 shows a good example of the intermittent behaviour of the flow by exhibiting two very different flow states at position $x/L \approx 0.45$ separated in time by only 1.7 s. A highly dynamic flow, most likely associated with a previously occurred thermal pluming event (Fig. 10), is carried downstream with the convection velocity of the boundary layer returning the boundary layer flow to a quieter state that closely resembles that of a laminar boundary layer.
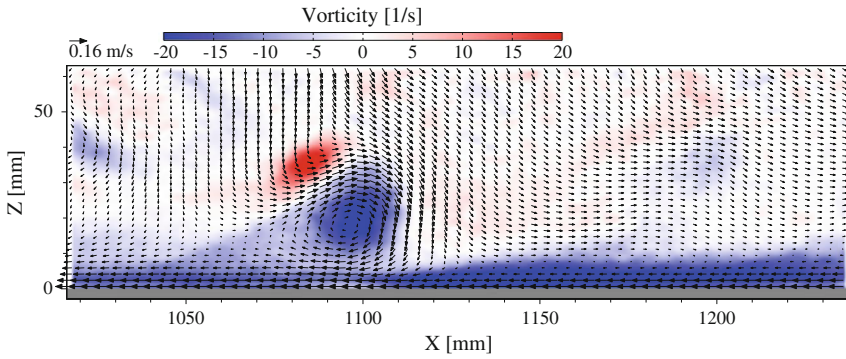
**Fig. 10** Thermal plume at $x/L = 0.5$. For better visibility, mean horizontal velocity of $0.16\,\text{m/s}$ has been subtracted; vectors are downsampled $4\times$ horizontally and $2\times$ vertically
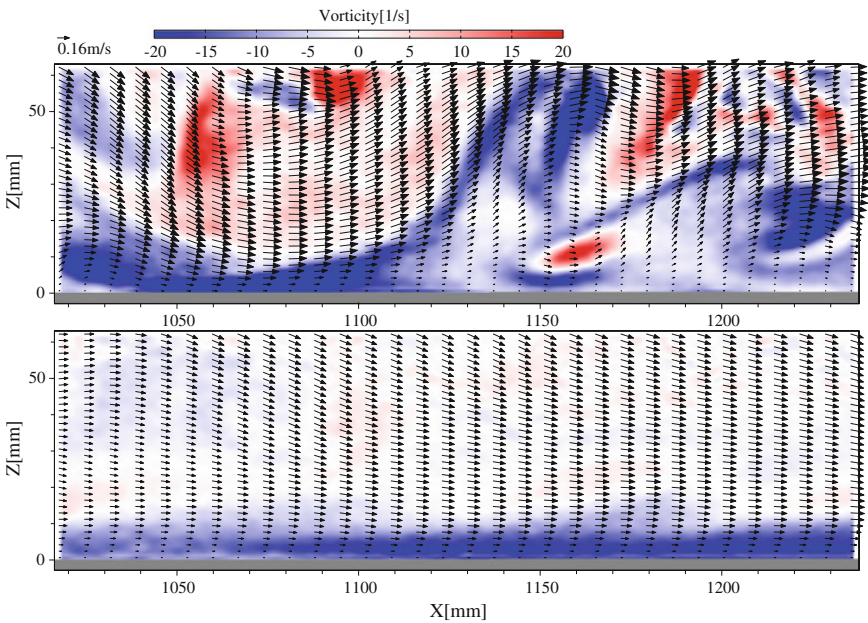


**Fig. 11** Two flow conditions at position $x/L = 0.5$ separated by $1.7\,\text{s}$ in time. Vectors are downsampled $8\times$ horizontally and $2\times$ vertically

The intermittent behaviour of the boundary layer flow is clearly visible in the time trace of normalized velocity $u/U_{\text{max}}$ and vorticity $\omega/\hat{\gamma}_w$ provided in Fig. 12. The time trace was obtained at a wall distance of $z/\delta = 1$ at sampling position B, $x/L = 0.48$. The red and green vertical lines in Fig. 12, right, correspond to the time instances for the flow maps presented in Fig. 11. In particular, the vorticity $z/\delta = 1$
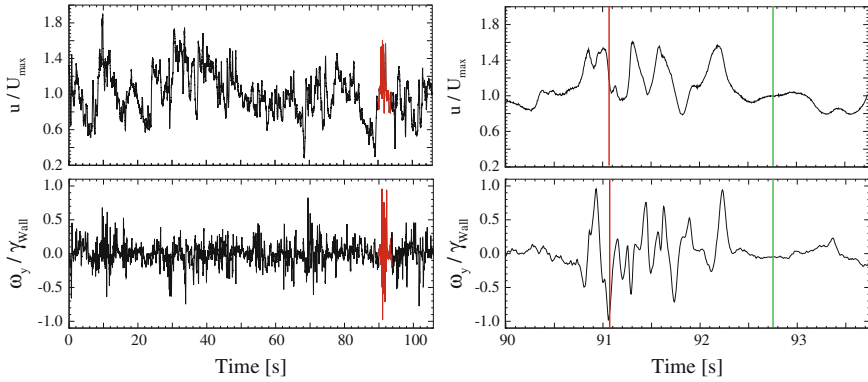
**Fig. 12** Time traces of normalized velocity $u/U_{\max}$ (*top*) and normalized vorticity $\omega/\dot{\gamma}_w$ (*bottom*) at position $x/L = 0.48$ and $z/\delta = 1$. Portion highlighted in *red* on left plot is magnified in right plot. *Red* and *green vertical lines* correspond to Fig. 11 *top* and *bottom*, respectively
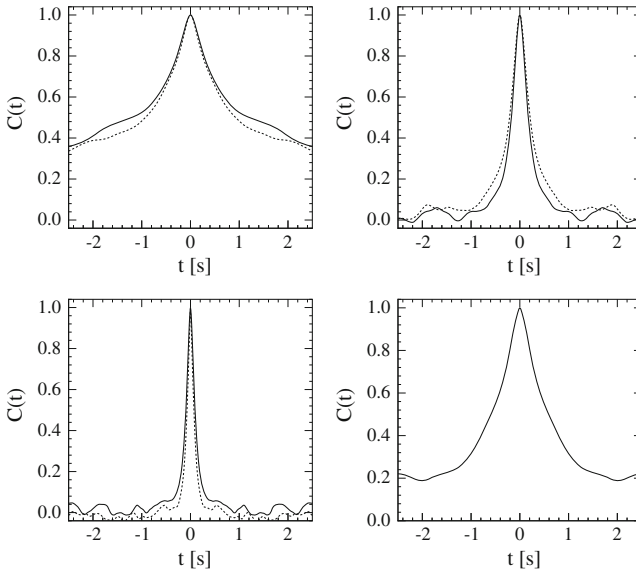


**Fig. 13** Autocorrelation functions at position $x/L = 0.64$ for velocity components $u$ and $w$ (*top row*), vorticity $\omega_y$ (*bottom left*) and wall shear rate $\dot{\gamma}_w$ (*bottom right*) for wall distances $z/\delta = 1$ (——) and $z/\delta = 1.8$ (- - - -)

exhibits a period of strong bursts with amplitudes reaching that of the mean wall shear rate.

The temporal correlation of selected flow components at selected locations provides some information on the time scales within the boundary layer and the interaction between different quantities. The autocorrelation of both velocity components
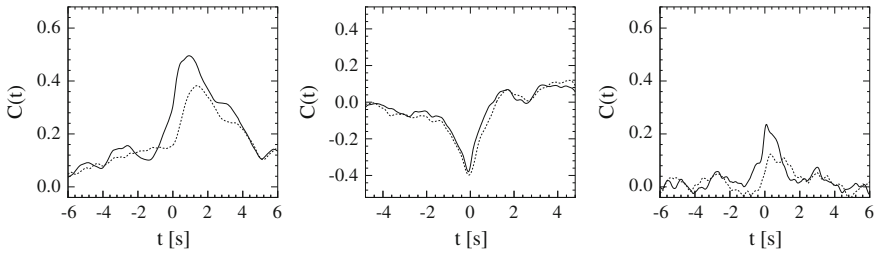
**Fig. 14** Cross-correlation functions at position $x/L = 0.64$ between wall shear rate $\dot{\gamma}_w$ and velocity components $u$ (*left*) and $w$ (*middle*), and vorticity $\omega_y$ (*right*) for wall distances $z/\delta = 1$ (——) and $z/\delta = 1.8$ (- - - -)

$u$ and $w$, the out-of-plane vorticity $\omega_y$ and the wall shear rate $\dot{\gamma}_w$ are shown in Fig. 13. Among these, the vorticity has the shortest time scale, which is due to their convection with the mean flow. The horizontal velocity component has the highest self-correlation of several seconds which is related to the rather steady horizontal motion of the flow. The self-correlation of the wall shear rate has a duration of roughly 1 s. The cross-correlations of velocity and vorticity with wall shear are depicted in Fig. 14. Here, the vortex structures convected with the bulk of the boundary layer have limited influence on the wall shear rate. On the other hand, both velocity components of the bulk flow have a pronounced influence on the wall shear. While the correlation with horizontal velocity component shows temporal lag of 1–2 s, the response of the wall shear to vertical motions is essentially without delay. This interaction seems independent of the velocity sampling position from the wall, which suggests that the wall shear rate is forced from the outside by the bulk flow of the RBC (e.g. falling plumes, impinging jets).

## 4.1 Statistical Convergence of the Data

When plotted side-by-side, the time-averaged data domains exhibit discontinuities at the borders. This indicates that the mean flow is not stationary between the acquisitions of the individual sequences (30 min between individual sequences). Variations in the fluctuations further indicate that the statistics are not fully converged, in spite of the rather considerable length of the sequences. For the given operating conditions and geometry of the RB cell, a free-fall velocity $U_f = (g \, \alpha \, \Delta T \, H)^{0.5}$ can be estimated at $U_f \approx 68.3$ mm/s with a corresponding free-fall time of $T_f = H/U_f \approx 36$ s. The mean data for the local overviews covers about $3 \, T_f$. On the other hand, Emran and Schumacher[7] estimate the average loop time of Lagrangian tracers at $20 \, T_f$, corresponding to a duration of 12 min. This is nearly achieved for the high-resolution profile PIV measurements at position B ($x/L = 0.48$). Laser Doppler measurements for similar configurations reported by du Puits et al. [2] and Li et al. [10] sampled

each point for up to 1 h and longer.[1] A comparable PIV measurement using the imaging configuration reported herein would require 360,000 images if sampled at 100 Hz corresponding to 400 GB of 8bit raw image data, if temporal coherence is to be preserved.

## 5 Summary and Conclusions

The velocity field close to the bottom horizontal plate in turbulent Rayleigh Bénard convection in air has been studied experimentally using long sequences of time-resolved PIV data. To the knowledge of the authors, these are the first PIV boundary layer measurements of RBC in air.

Whether the RBC boundary layer flow is turbulent or not cannot be answered conclusively. On the one hand, the Reynolds number of Re = 265 is below the critical threshold of Re = 420. The lack of a log-law region in the velocity profile is another indication that the boundary layer is not turbulent. Furthermore, a shape factor of $S = 2.2$–$2.35$ is closer to that of the laminar Prandtl-Blasius solution with $S \approx 2.5$ rather than that of a turbulent boundary layer or wall jet with $S = 1.3$–$1.4$. On the other hand, the flow is highly intermittent with significant velocity variations (>30 % at half the mean kinematic boundary layer thickness).

As shown in Fig. 6, right, the peak horizontal fluctuations are observed at $\approx 16\, z^+$ ($z/\delta = 0.5$) which is significantly more than for RBC measurements in water at similar Rayleigh number [12] and is closer to the value of $12\, z^+$ for classical flat-plate boundary layers. The difference to the measurements in water can be related to the much thicker thermal boundary layer in air, which is of similar magnitude as the kinematic boundary layer [11] while it is confined to the viscous sublayer in water [12]. Therefore, the interaction of turbulent structures from the mean wind with the boundary layer will not only destabilize the inner shear of the kinematic boundary layer, but will also destabilize the thermal boundary layer. This is substantiated by the cross-correlation functions between wall shear rate and outer flow (Fig. 14) which show that in particular, vertical motions of the outer flow directly act all the way into the viscous sublayer. This is in agreement with similar conjectures reported in the literature that the wall-normal forcing is more dominant than wall-parallel direction forcing [14]. This vertical forcing results from buoyancy effects that manifest themselves in the form of plume impingement and detachment. In essence, both contributions, inner shear and external forcing of the boundary layer, must be considered when predicting the critical bound towards the "ultimate regime" of thermal convection [9].

---

[1]du Puits et al. [2] reported on 48 h hot-film measurements in the RB cell and observed a 30 % variation of the typical mean velocity over a duration of about 5 h.

# References

1. G. Ahlers, S. Grossmann, D. Lohse, Heat transfer and large scale dynamics in turbulent Rayleigh-Bénard convection. Rev. Mod. Phys. **81**, 503–537 (2009). doi:10.1103/RevModPhys.81.503

2. R. du Puits, C. Resagk, A. Thess, Mean velocity profile in confined turbulent convection. Phys. Rev. Lett. **99**, 234504 (2007). doi:10.1103/PhysRevLett.99.234504

3. R. du Puits, C. Resagk, A. Thess, Structure of viscous boundary layers in turbulent Rayleigh-Bénard convection. Phys. Rev. E **80**, 036318 (2009). doi:10.1103/PhysRevE.80.036318

4. R. du Puits, J. Rilk, C. Resagk, A. Thess: Boundary layers in turbulent Rayleigh-Bénard convection in air. (2012). arXiv:1209.6201v1[physics.fluspsdyn]

5. R. du Puits, C. Resagk, A. Thess, Thermal boundary layers in turbulent Rayleigh-Bénard convection at aspect ratios between 1 and 9. New J. Phys. **15**(1), 013040 (2013)

6. R. du Puits, L. Li, C. Resagk, A. Thess, C. Willert, Turbulent boundary layer in high Rayleigh number convection in air. Phys. Rev. Lett. **112**, 124301 (2014). doi:10.1103/PhysRevLett.112.124301

7. M.S. Emran, J. Schumacher, Lagrangian tracer dynamics in a closed cylindrical turbulent convection cell. Phys. Rev. E **82**, 016303 (2010). doi:10.1103/PhysRevE.82.016303

8. S. Grossmann, D. Lohse, Scaling in thermal convection: a unifying theory. J. Fluid Mech. **407**, 27–56 (2000). doi:10.1017/S0022112099007545

9. R.H. Kraichnan, Turbulent thermal convection at arbitrary prandtl number. Phys. Fluid (1958-1988) **5**(11), 1374–1389 (1962). doi:10.1063/1.1706533

10. L. Li, C. Resagk, R. du Puits, Viscous boundary layers in turbulent Rayleigh-Bénard convection. J. Phys.: Conf. Ser. **318**(8), 082004 (2011). doi:10.1088/1742-6596/318/8/082004

11. N. Shi, M.S. Emran, J. Schumacher, Boundary layer structure in turbulent Rayleigh-Bénard convection. J. Fluid Mech. **706**, 5–33 (2012). doi:10.1017/jfm.2012.207

12. C. Sun, Y.H. Cheung, K.Q. Xia, Experimental studies of the viscous boundary layer properties in turbulent Rayleigh-Bénard convection. J. Fluid Mech. **605**, 79–113 (2008). doi:10.1017/S0022112008001365

13. W. Tollmien, Über die Entstehung der Turbulenz. 1. Mitteilung. Nachrichten von der Gesellschaft der Wissenschaften zu Göttingen. Mathematisch-Physikalische Klasse **1929**, 21–44 (1929)

14. M. van Reeuwijk, H.J.J. Jonker, K. Hanjalić, Wind and boundary layers in Rayleigh-Bénard convection. ii. Boundary layer character and scaling. Phys. Rev. E **77**, 036312 (2008). doi:10.1103/PhysRevE.77.036312

15. C. Willert, High-speed particle image velocimetry for the efficient measurement of turbulence statistics. Exp. Fluids (submitted)

16. Q. Zhou, K.Q. Xia, Measured instantaneous viscous boundary layer in turbulent Rayleigh-Bénard convection. Phys. Rev. Lett. **104**, 104301 (2010). doi:10.1103/PhysRevLett.104.104301